

# Estimation of absolute stress in the hypocentral region of the 2019 Ridgecrest, California, earthquakes

Yuri Fialko (✉ [yfialko@ucsd.edu](mailto:yfialko@ucsd.edu))

Scripps Institution of Oceanography <https://orcid.org/0000-0002-6161-8467>

---

## Research Article

**Keywords:** Principal Stress Axes, Focal Mechanism Data, Conjugate Faults, Deviatoric Stress, Frictional Strength

**Posted Date:** October 13th, 2020

**DOI:** <https://doi.org/10.21203/rs.3.rs-75177/v1>

**License:**  This work is licensed under a Creative Commons Attribution 4.0 International License.

[Read Full License](#)

---

**Version of Record:** A version of this preprint was published at Journal of Geophysical Research: Solid Earth on July 1st, 2021. See the published version at <https://doi.org/10.1029/2021JB022000>.

# 1 Estimation of absolute stress in the hypocentral region of the 2 2019 Ridgecrest, California, earthquakes

3 Yuri Fialko

4 *Institute of Geophysics and Planetary Physics, Scripps Institution of Oceanography, University of*  
5 *California San Diego, La Jolla, CA*

6 Strength of the upper brittle part of the Earth’s lithosphere controls defor-  
7 mation styles in tectonically active regions, surface topography, seismicity, and  
8 the occurrence of plate tectonics, yet remains one of the least constrained and  
9 most debated quantities in geophysics. Seismic data (in particular, earthquake  
10 focal mechanisms) have been used to infer orientation of the principal stress  
11 axes. Here I show that the focal mechanism data can be combined with infor-  
12 mation from precise earthquake locations to place robust constraints not only  
13 on the orientation, but also on the magnitude of absolute stress at depth. The  
14 proposed method uses machine learning to identify quasi-linear clusters of seis-  
15 micity associated with active faults. A distribution of the relative attitudes of  
16 conjugate faults carries information about the amplitude and spatial heterogene-  
17 ity of the deviatoric stress and frictional strength in the seismogenic zone. The  
18 observed dihedral angles between active conjugate faults in the Ridgecrest (Cal-  
19 ifornia, USA) area that hosted a recent sequence of strong earthquakes suggests  
20 the effective coefficient of friction of 0.4-0.6, and depth-averaged shear stress on  
21 the order of 25-40 MPa, intermediate between predictions of the “strong” and  
22 “weak” fault theories.

23 There is a long-standing debate regarding the level of average shear stress in the Earth’s  
24 crust<sup>1-4</sup>. Estimates of earthquake stress drops place a lower bound on shear stress resolved on  
25 seismogenic faults on the order of 1 - 10 MPa<sup>5,6</sup>. Laboratory measurements of quasi-static  
26 rock friction<sup>7-10</sup>, orientation of young faults with respect to the inferred principal stress  
27 axes<sup>11,12</sup>, and measurements in deep boreholes in stable intraplate interiors<sup>13,14</sup> suggest that

28 the brittle upper crust should be able to support much higher deviatoric stresses on the  
29 order of lithostatic pressure ( $> 100$  MPa for  $\sim 15$  km thick seismogenic zone), provided  
30 that the pore fluid pressure is approximately hydrostatic. Extrapolation of the laboratory  
31 measurements of quasi-static friction to in situ rock failure, and the assumption of hydrostatic  
32 pore pressure constitute the so-called “strong fault” theory<sup>4,7</sup>.

33 In contrast, unfavorable orientation of some mature faults with respect to the principal  
34 stress axes<sup>15-17</sup>, the “heat flow paradox” of the San Andreas Fault<sup>18</sup>, high degree of slip  
35 localization on exhumed faults<sup>19,20</sup>, a possibility of fluid over-pressurization<sup>21</sup>, low frictional  
36 strength of some parts of mature faults suggested by scientific drilling experiments<sup>22</sup>, and  
37 strong dynamic weakening observed in laboratory friction experiments at slip rates in excess  
38 of  $\sim 0.1$  m/s<sup>23-25</sup> lend support to the “weak fault” theory according to which faults may  
39 operate at background deviatoric stresses well below the failure envelope predicted by the  
40 Byerlee’s law<sup>26,27</sup>. Low effective friction on major plate boundary faults is also required by  
41 geodynamic models of large-scale tectonic phenomena such as subduction and orogeny<sup>28-30</sup>.

42 One possible explanation reconciling disparate views on the magnitude of deviatoric  
43 stresses in the lithosphere is that the effective fault strength may depend on fault “age”,  
44 or total offset: young developing faults may be relatively strong while mature well-slipped  
45 faults may be weak, possibly because of activation of various weakening mechanisms with  
46 an increasing cumulative slip<sup>20,27</sup>. However, conditions that govern such a transition, and  
47 the evolution of fault strength as a function of cumulative offset are still poorly known.

48 Our understanding of the fault strength problem is severely limited by the lack of mea-  
49 surements of deviatoric stress at seismogenic depths. Apart from a scarce set of point mea-  
50 surements in deep boreholes<sup>1,22</sup>, most of the available information is derived from analyses  
51 of seismic data. The most commonly used method of “stress inversion” relies on earthquake  
52 focal mechanisms to solve for the orientations of principal stress axes that are most consis-  
53 tent with all of the focal mechanisms in a specified volume<sup>3,31,32</sup>. This method however is  
54 unable to evaluate the magnitude of deviatoric stress.

55 Inversions for the orientation of principal stress axes require a diverse set of focal mech-  
56 anisms which, along with the assumption of a locally constant stress, implies heterogeneity  
57 in the effective fault strength<sup>33</sup>. Here I show that the magnitude of deviatoric stress can  
58 be estimated by quantifying a distribution of fault orientations with respect to one of the  
59 principle stress axes, or between sets of conjugate faults activated by a given ambient stress.  
60 I illustrate this using data from the Eastern California Shear Zone (ECSZ) that hosted a  
61 series of strong earthquakes near the town of Ridgecrest in July of 2019<sup>34-36</sup>, and provide  
62 quantitative estimates on the magnitude of shear stress resolved on seismogenic faults in the  
63 Ridgecrest area.

64 The July 2019 Ridgecrest, California earthquakes ruptured a system of right and left-  
65 lateral strike-slip faults in the northern part of the ECSZ (Supplementary figure S1), with  
66 the largest event having magnitude 7.1<sup>34-36</sup>. The ECSZ is an emergent plate boundary  
67 that accommodates an increasing fraction of relative motion between the Pacific and North  
68 American plates since its inception 6-10 Ma ago<sup>37-40</sup>. As such, the ECSZ is a natural  
69 laboratory for studying the development and evolution of new (and re-activation of old)  
70 fault systems.

71 The nearly perpendicular orientation of conjugate faults ruptured by the Ridgecrest  
72 earthquakes (Figure S1b) is distinctly different from optimal orientations predicted by the  
73 strong fault theory (dihedral angles of 50-60 degrees for the coefficient of friction of 0.6-  
74 0.8)<sup>4,26</sup>. This prompted suggestions that in situ coefficient of friction is close to zero<sup>34</sup>.  
75 Alternatively, high-angle conjugate faults could result from rotation away from the optimal  
76 orientation since the initiation of the ECSZ<sup>41</sup>. A pattern of high-angle faulting similar to  
77 that involved in the 2019 earthquake sequence is prevalent in a broader region around the  
78 2019 ruptures (Figure S1a). The observed range of fault strikes can be used to constrain the  
79 magnitude of deviatoric stress, as the latter controls conditions for activation and suppression  
80 of slip on new as well as pre-existing faults<sup>26</sup>. The focal mechanism data alone are not suitable  
81 for this purpose because of two fundamental limitations. First, typical errors in the fault

82 plane solutions of 20-30 degrees<sup>35,42</sup> are too large to resolve differences between optimal and  
83 non-optimal fault orientations. Second, an intrinsic ambiguity between the two nodal planes  
84 in a focal mechanism does not allow one to isolate sets of synthetic vs antithetic faults.

85 The above limitations can be mitigated by combining information provided by focal  
86 mechanisms with geometric constraints from well-determined earthquake hypocenters. Pre-  
87 cisely relocated seismicity catalogs reveal ubiquitous lineated clusters of earthquakes that  
88 illuminate faults or fault segments of various sizes and orientations (Figure S1a). I use  
89 earthquake lineations to map the distribution and attitude of active faults throughout the  
90 seismogenic layer. Details of the procedure are described in the Supplementary Materials.  
91 In case of sufficiently localized clusters of microearthquakes, fault strikes can be determined  
92 with accuracy up to several degrees, an order of magnitude improvement over the individ-  
93 ual focal mechanism solutions. Also, fault orientations (well defined by seismicity lineations)  
94 along with polarity of focal mechanisms uniquely constrain the sense of slip on the respective  
95 faults.

96 Figure 1 shows quasi-linear clusters of micro-earthquakes identified in the background  
97 (prior to July 2019) seismicity data using a machine learning algorithm (see Supplementary  
98 Materials; Figures S2-S4). For each cluster, I compute a composite focal mechanism by  
99 summing moment tensors of all events in a cluster. The resulting composite focal mechanisms  
100 are predominantly strike-slip, with approximately north-south P-axis, consistent with results  
101 of inversions for principle stress and strain rate axes<sup>35,41,44</sup>.

102 The observed distribution of orientations of active faults in the Ridgecrest-Coso area  
103 prior to the 2019 earthquake sequence is shown in Figure 2. Using information from both  
104 the fault strike (constrained by seismicity lineations) and rake (constrained by the compos-  
105 ite focal mechanisms) data, one can identify right- and left-lateral faults in the total fault  
106 population without any assumptions about the sense of shear stress resolved on the respec-  
107 tive faults due to regional tectonic loading. The two sets of conjugate faults form distinct  
108 clusters in a polar histogram (red and blue sectors in Figure 2). Left-lateral faults are well

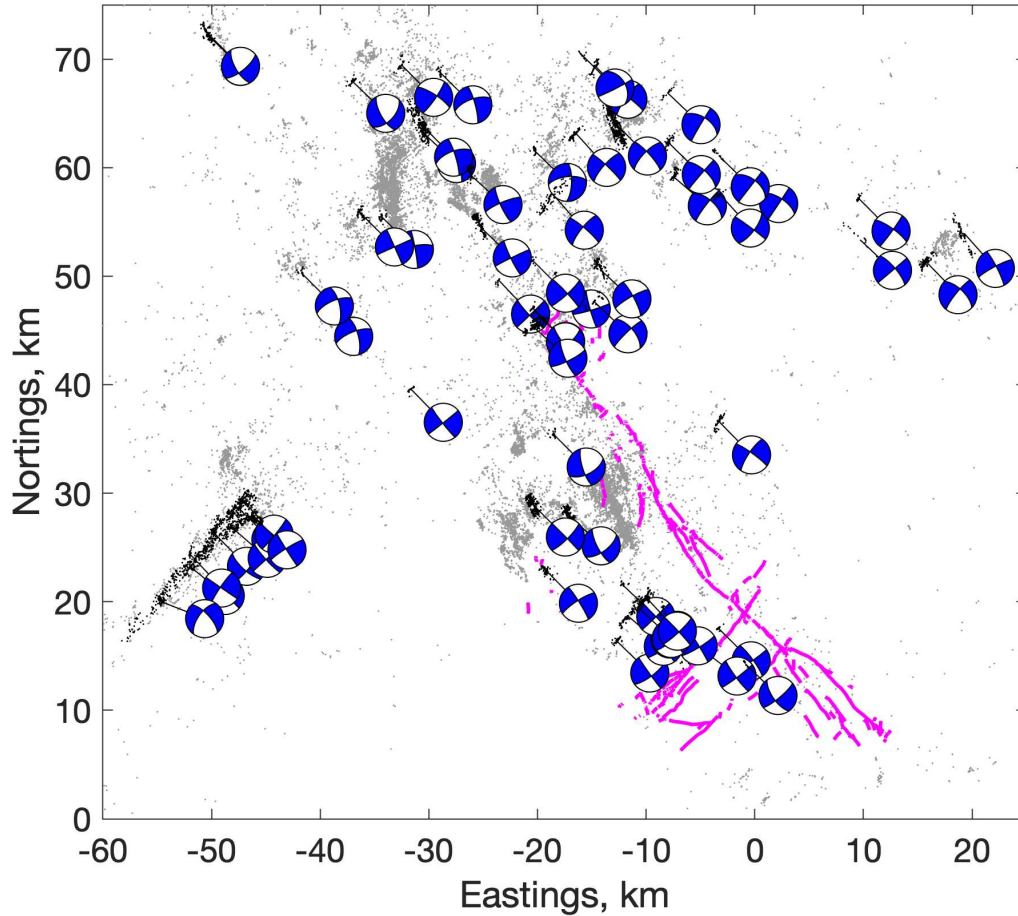


Figure 1: Map of the Ridgecrest-Coso area. Magenta wavy lines denote surface traces of the 2019 ruptures mapped by field surveys<sup>43</sup>. Grey dots denote pre-earthquake (1981-2019) seismicity from the focal mechanism catalog<sup>42</sup>. Black dots denote seismicity lineations selected by the clustering algorithm (see Supplementary Materials and Figures S2-S4 for details). White and blue “beach balls” denote the best-fitting double-couple composite focal mechanism for the respective linear clusters of earthquakes. Local origin is at  $117.5^{\circ}\text{W}$ ,  $35.5^{\circ}\text{N}$ .

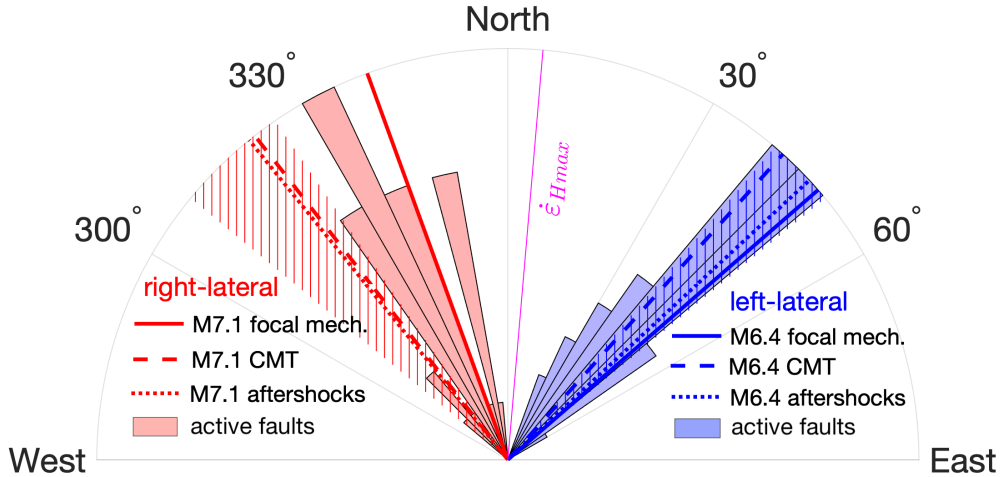


Figure 2: A distribution of strikes of 65 active fault segments shown in Figure 1. Red histogram corresponds to right-lateral faults (total of 28 samples, maximum number of samples per bin: 7), and blue histogram corresponds to left-lateral faults (total of 37 samples, maximum number of samples per bin: 9). Hatched areas denote orientation of faults ruptured by the M6.4 foreshock and M7.1 mainshock of the 2019 sequence<sup>36,41</sup>. Thin magenta line denotes the principal shortening rate axis derived from secular GPS velocities<sup>41</sup>.

109 aligned with those ruptured during the July 4 2019 M6.4 foreshock. Right-lateral faults  
 110 trend somewhat more northerly compared to the main rupture of the July 5 2019 main-  
 111 shock, but similar to the initial rupture at the hypocenter of the mainshock suggested by the  
 112 first motion data<sup>36,41</sup>. The axis of the principal shortening rate<sup>41</sup> approximately bisects the  
 113 dihedral angles formed by the conjugate fault planes (Figure 2). The principal compression  
 114 axis is oriented similarly to the principal shortening rate axis ( $\sim 5$  degrees east of north)  
 115 around the hypocentral area of the M7.1 mainshock<sup>35,41</sup>.

116 To further quantify the range of admissible orientations of conjugate faults, I calculate  
 117 a dihedral angle between every pair of the identified conjugate faults. Uncertainties in  
 118 dihedral angles were computed using errors in the estimated fault strikes, as described in the  
 119 Supplementary Materials. Figure 3 shows a histogram of the dihedral angles  $2\theta$ , where  $\theta$  is an  
 120 angle between either fault plane and a bisect. The distribution shown in Figure 3 has a peak  
 121 around 70 degrees, and lower and upper bounds around 30 and 100 degrees, respectively.  
 122 Assuming a homogeneous background stress, some of the conjugate faults are optimally

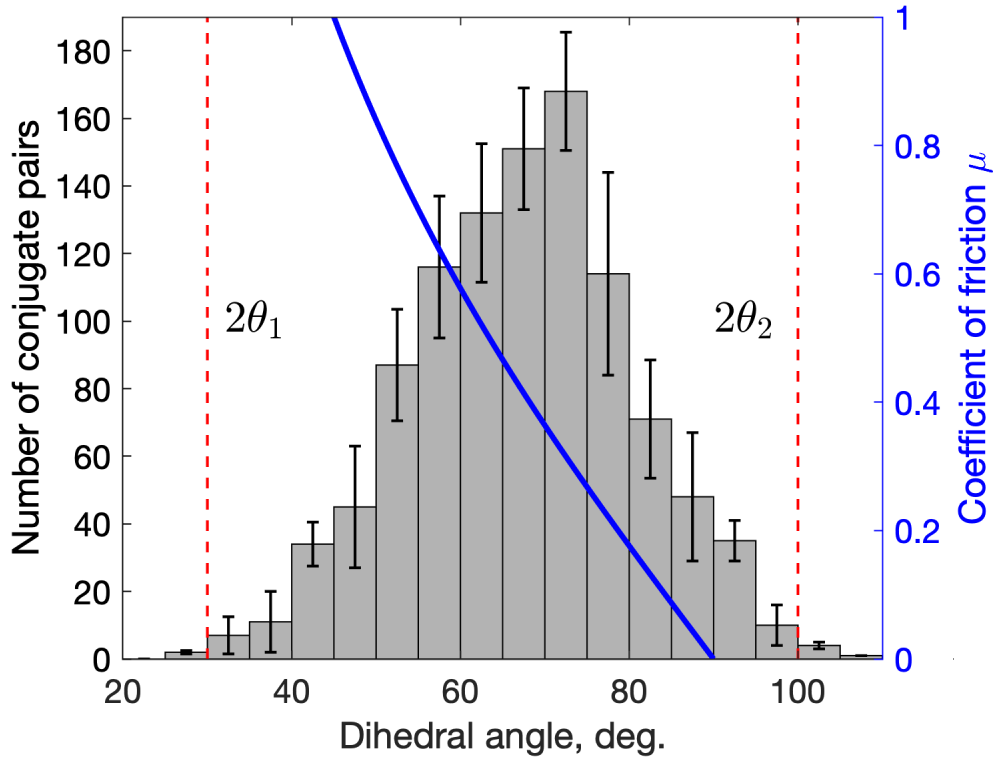


Figure 3: A histogram of dihedral angles between the conjugate strike-slip faults identified in Figure 1. Red vertical lines denote the lower ( $2\theta_1$ ) and upper ( $2\theta_2$ ) bounds on the observed distribution. Blue line (right axis) denotes the coefficient of friction corresponding to conjugate faults that are optimally oriented for failure according to the Mohr-Coulomb criterion,  $\mu = 1/\tan(2\theta)$ <sup>26</sup>.

123 oriented for failure given the laboratory values of the coefficient of friction  $\mu \sim 0.6 - 0.8$ ,  
124 while others are not optimally oriented for any reasonable value of  $\mu$ .

125 To test whether results presented in Figures 2 and 3 could be affected by stress het-  
126 erogeneity, I examine a distribution of angles between synthetic faults (i.e., subsets of faults  
127 that have the same sense of slip) as a function of distance between the faults (Figure S5).  
128 The data indicate that (i) there is a notable diversity in fault orientations at short ( $< 10$   
129 km) distances, (ii) there is little, if any, systematic increase in the diversity of fault ori-  
130 entations with distance, and (iii) fault orientations exhibit coherence at large ( $> 30$  km)  
131 distances. These findings argue in favor of local heterogeneities in the fault strength rather  
132 than the background stress. Previous studies suggested a local rotation of the principal  
133 stress axes around the Coso region (northings  $N > 40$  km in a local coordinate system  
134 used in Figure 1)<sup>35</sup>. To investigate the respective possibility, I divided the data into the  
135 northern ( $N > 40$  km) and southern ( $N < 40$  km) sub-sets, and repeated the analysis for  
136 each sub-set. Figures S6-S7 show the variability in fault strikes vs distance between pairs  
137 of synthetic faults, and Figures S8-S9 show the distribution of fault strikes. The northern  
138 sub-set shows some correlation between the diversity of fault strikes and distance between  
139 synthetic faults, suggesting a possible role of stress heterogeneity (Figure S6). In part such  
140 heterogeneity might be attributed to fluid pumping at the Coso geothermal plant<sup>40,45</sup>. Also,  
141 conjugate faults in the northern sub-set exhibit smaller dihedral angles that are closer to op-  
142 timal orientations compared to faults in the southern sub-set (Figures S8 and S9). However,  
143 the mean of the left- and right-lateral fault strikes (i.e., the average bisect) is not resolvably  
144 different between the northern and southern sub-sets, suggesting that a constant regional  
145 stress is a viable first-order approximation, in particular for the hypocentral region of the  
146 2019 earthquakes.

147 It may be argued that small earthquakes that comprise linear clusters (Figures 1, S1a  
148 and S2-S4) are primarily governed by the rate and state friction and are not subject to  
149 strong dynamic weakening, so that the peak yield stress is comparable to the background

150 stress<sup>20</sup>. In this case, one can interpret the observed range of fault orientations (Figure 3)  
 151 in terms of activation ( $\theta > \theta_1$ ) and de-activation ( $\theta > \theta_2$ ) of pre-existing or newly created  
 152 faults. It is generally recognized that the continental Earth's crust is pervasively faulted  
 153 and contains cracks, fractures and other structural defects that can serve as potential slip  
 154 surfaces over a broad range of sizes and orientations<sup>26,46</sup>. A condition for activation of  
 155 a fault oriented at an angle  $\theta$  with respect to the principal compression axis is given by  
 156  $\sigma'_1(1 - \mu \tan \theta) = \sigma'_3(1 + \mu \cot \theta)$ , where  $\sigma'_1$  is the effective maximum compressive stress  
 157 (maximum compressive stress minus the pore pressure  $P$ ), and  $\sigma'_3$  is the effective minimum  
 158 compressive stress<sup>26</sup>.

159 The above relationship is typically under-determined as the number of unknowns (e.g.,  
 160  $\sigma'_1$ ,  $\sigma'_3$  and  $\mu$ ) is greater than the number of observables (e.g., the angle between conjugate  
 161 faults or faults and the principal stress axes). In case of the Ridgecrest seismicity, sev-  
 162 eral unique conditions allow one to resolve this uncertainty. First, a transtensional stress  
 163 regime manifested by a mix of strike-slip and normal focal mechanisms<sup>35</sup>, including spa-  
 164 tially overlapping strike-slip and normal earthquake ruptures<sup>36</sup> indicates that the maximum  
 165 compressive ( $\sigma'_1$ ) and intermediate ( $\sigma'_2$ ) principle stresses are of essentially the same magni-  
 166 tude. In this case, both should approximately equal the effective lithostatic stress,  $\rho_c g z - P$ ,  
 167 where  $\rho_c$  is the average density of the upper crust,  $g$  is the gravitational acceleration, and  
 168  $z$  is depth. For a given  $\sigma'_1$ , the least compressive stress  $\sigma'_3$  and the effective coefficient  
 169 of friction  $\mu_1$  can be found from the observed distribution of orientations of active faults  
 170 ( $\theta_1 < \theta < \theta_2$ , Figure 3),  $\mu_1 = 1/\tan(\theta_1 + \theta_2)$  and  $\sigma'_3 = \sigma'_1/R$ , where  $R$  is the stress ratio  
 171 given by  $R = (1 + \mu_1 \cot \theta_1)/(1 - \mu_1 \tan \theta_1) = (1 + \mu_1 \cot \theta_2)/(1 - \mu_1 \tan \theta_2)$ . The effec-  
 172 tive coefficient of friction  $\mu_1$  provides a lower bound on frictional strength of re-activated  
 173 sub-optimally oriented faults. Faults that are oriented at more acute angles with respect  
 174 to the principal compression axis can be on the verge of failure if they have a higher co-  
 175 efficient of friction, with an upper bound  $\mu_0$  that corresponds to an optimal orientation,  
 176  $\mu_0 = 0.5(R - 1)/\sqrt{R}$  (see Supplementary Materials).

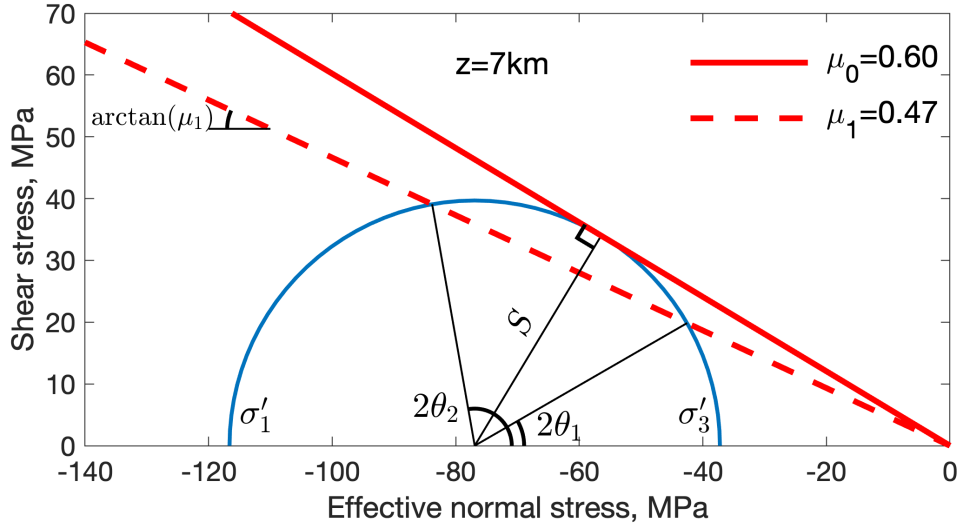


Figure 4: The estimated state of stress in the hypocentral region of the 2019 Ridgecrest earthquakes. Blue curve (the Mohr circle) denotes variations in shear stress on potential slip planes as a function of a dihedral angle  $2\theta$  between conjugate slip planes (or angle  $\theta$  between a slip plane and the maximum compression axis). Radius of the Mohr circle represents the maximum shear stress,  $S = |\sigma'_1 - \sigma'_3|/2$ . Red lines are the Mohr-Coulomb failure envelopes corresponding to activation of pre-existing faults ( $\mu_1$ , dashed line), and generation of new faults ( $\mu_0$ , solid line). Calculations assume  $\rho_c = 2.7 \times 10^3 \text{ kg/m}^3$ ,  $\rho_w = 10^3 \text{ kg/m}^3$ , and  $g = 9.8 \text{ m/s}^2$ .

177 Figure 4 shows a Mohr circle diagram for the state of stress that satisfies the above  
 178 conditions as well as the assumption of a hydrostatic pore pressure ( $P = \rho_w g z$ , where  $\rho_w$  is  
 179 the density of water), at a reference depth of 7 km. The latter is within the estimated range  
 180 of hypocentral depths of the M7.1 mainshock (3-8 km)<sup>35</sup>. It also approximately corresponds  
 181 to the middle of the seismogenic layer, so that absolute stresses shown in Figure 4 represent  
 182 stresses averaged over the thickness of the seismogenic layer. As one can see from Figure 4,  
 183 the estimated stress ratio is  $R \approx 3$ , the depth-averaged shear stresses resolved on seismically  
 184 active faults are 25-40 MPa, and the admissible range for the in situ coefficient of friction is  
 185  $0.4 < \mu < 0.6$ .

186 High-end values of the estimated coefficient of friction are in agreement with laboratory  
 187 measurements of quasi-static friction of most rock types<sup>7,47</sup>, and may correspond to new

188 faults forming in the ECSZ (Figure 4). The value of  $\mu \sim 0.6$  is also consistent with models  
189 suggesting that faults ruptured in the 2019 sequence were initiated at an optimal orientation  
190 of  $\sim 30^\circ$  with respect to the principal compression axis at the inception of the ECSZ,  
191 and gradually weakened as they continued to accumulate slip and rotate away from the  
192 optimal orientation due to long-term tectonic motion<sup>41</sup>. Hauksson and Jones<sup>35</sup> proposed  
193 that orientation of the 2019 earthquake ruptures with respect to the principal compression  
194 axis might be explained assuming higher values of the stress ratio ( $R > 5$ ) and the coefficient  
195 of friction ( $\mu = 0.75$ ). Such high values however would be inconsistent with the observed  
196 transtensional stress regime in the Ridgecrest-Coso area, and/or require pore fluid pressures  
197 close to the least compressive stress. Also, a high coefficient of friction would imply a peak  
198 in dihedral angles of the regional fault population around the respective optimal value ( $\sim 55$   
199 degrees for  $\mu = 0.75$ ) which is not observed (Figure 3). Note orientations of the 2019 ruptures  
200 are within the range of a regional data set (Figure 3), so that results presented in this study  
201 apply to the observed geometry of the 2019 earthquakes.

202 At the low end, the inferred values of depth-averaged shear stress on sub-optimally ori-  
203 ented faults ( $\sim 25$  MPa) may be indicative of an onset of various weakening mechanisms  
204 such as mineral alteration, ultra-comminution, pressurization of fault zone fluids, and per-  
205 haps dynamic weakening (for the largest events produced by the identified active faults<sup>36</sup>).  
206 The low-end values of shear stress on faults in the ECSZ around Ridgecrest are similar to  
207 values estimated on the San Andreas Fault (SAF) using heat flow data<sup>18</sup> and stress per-  
208 turbations due to topography<sup>48</sup>. Despite similar values of the driving shear stress, active  
209 faults in the Ridgecrest area are still relatively strong compared to the SAF because of the  
210 transtensional stress regime in the ECSZ versus transpressional regime on the SAF. Never-  
211 theless, results presented in this study suggest that a transition from “strong” to “weak”  
212 faults may initiate at the early stages of formation of a plate boundary, and involve relatively  
213 low total offsets.

214 **Acknowledgments.** We thank reviewers... This study was supported by NSF (grant EAR-  
215 1841273) and NASA (grant 80NSSC18K0466). Figures were produced using Generic Mapping Tools  
216 (GMT)<sup>49</sup> and Matlab.

## 217 References

- 218 **1** Zoback, M. *et al.* New evidence on the state of stress of the San- Andreas fault system. *Science*  
219 **238**, 1105–1111 (1987).
- 220 **2** Rice, J. R. Fault stress states, pore pressure distribution, and the weakness of the San Andreas  
221 Fault. In Evans, B. & Wong, T. (eds.) *Fault mechanics and transport properties of rocks*,  
222 475–503 (Academic, San Diego, CA, USA, 1992).
- 223 **3** Hardebeck, J. L. & Hauksson, E. Crustal stress field in southern California and its implications  
224 for fault mechanics. *J. Geophys. Res.* **106**, 21859–21882 (2001).
- 225 **4** Scholz, C. H. *The mechanics of earthquakes and faulting* (3rd Ed., 493 pp., Cambridge Univ.  
226 Press, New York, NY, 2019).
- 227 **5** Choy, G. L. & Boatwright, J. L. Global patterns of radiated seismic energy and apparent stress.  
228 *J. Geophys. Res.* **100**, 18205–18228 (1995).
- 229 **6** Allmann, B. P. & Shearer, P. M. Global variations of stress drop for moderate to large earth-  
230 quakes. *J. Geophys. Res.* **114**, B01310 (2009).
- 231 **7** Byerlee, J. Friction of rock. *Pure Appl. Geophys.* **116**, 615–626 (1978).
- 232 **8** Marone, C. Laboratory-derived friction laws and their application to seismic faulting. *Annu.*  
233 *Rev. Earth Planet. Sci.* **26**, 643–696 (1998).
- 234 **9** Mitchell, E., Fialko, Y. & Brown, K. M. Temperature dependence of frictional healing of West-  
235 erly granite: experimental observations and numerical simulations. *Geochemistry, Geophysics,*  
236 *Geosystems* **14**, 567–582 (2013).
- 237 **10** Mitchell, E., Fialko, Y. & Brown, K. Frictional properties of gabbro at conditions corresponding  
238 to slow slip events in subduction zones. *Geochemistry, Geophysics, Geosystems* **16**, 4006–4020  
239 (2015).
- 240 **11** Walsh, J. & Watterson, J. Dips of normal faults in British Coal Measures and other sedimentary  
241 sequences. *Journal of the Geological Society* **145**, 859–873 (1988).
- 242 **12** Collettini, C. & Sibson, R. H. Normal faults, normal friction? *Geology* **29**, 927–930 (2001).
- 243 **13** Zoback, M. *et al.* Upper-crustal strength inferred from stress measurements to 6 km depth in  
244 the KTB borehole. *Nature* **365**, 633–635 (1993).
- 245 **14** Townend, J. & Zoback, M. How faulting keeps the crust strong. *Geology* **28**, 399–402 (2000).
- 246 **15** Mount, V. & Suppe, J. State of stress near the San Andreas fault: Implications for wrench  
247 tectonics. *Geology* **15**, 1143–1146 (1987).
- 248 **16** Wernicke, B. Low-angle normal faults and seismicity: A review. *J. Geophys. Res.* **100**, 20159–  
249 20174 (1995).
- 250 **17** Wang, K. & Fialko, Y. Observations and modeling of co- and postseismic deformation due to  
251 the 2015  $M_w$  7.8 Gorkha (Nepal) earthquake. *J. Geophys. Res.* **123**, 761–779 (2018).

- 252 **18** Lachenbruch, A. H. & Sass, J. H. Heat flow and energetics of the San Andreas fault zone. *J.*  
253 *Geophys. Res.* **85**, 6185–6222 (1980).
- 254 **19** Chester, J. S., Chester, F. M. & Kronenberg, A. K. Fracture surface energy of the Punchbowl  
255 fault, San Andreas system. *Nature* **437**, 133–136 (2005).
- 256 **20** Fialko, Y. Fracture and Frictional Mechanics - Theory. In Schubert, G. (ed.) *Treatise on*  
257 *Geophysics, 2nd. Ed., Vol. 4*, 73–91 (Elsevier Ltd., Oxford, 2015).
- 258 **21** Sibson, R. H. Controls on maximum fluid overpressure defining conditions for mesozonal min-  
259 eralisation. *J. Struct. Geol.* **26**, 1127–1136 (2004).
- 260 **22** Lockner, D. A., Morrow, C., Moore, D. & Hickman, S. Low strength of deep San Andreas fault  
261 gouge from SAFOD core. *Nature* **472**, 82–85 (2011).
- 262 **23** Di Toro, G. *et al.* Fault lubrication during earthquakes. *Nature* **471**, 494–498 (2011).
- 263 **24** Han, R., Hirose, T. & Shimamoto, T. Strong velocity weakening and powder lubrication of  
264 simulated carbonate faults at seismic slip rates. *J. Geophys. Res.* **115** (2010).
- 265 **25** Brown, K. M. & Fialko, Y. "Melt welt" mechanism of extreme weakening of gabbro at seismic  
266 slip rates. *Nature* **488**, 638–641 (2012).
- 267 **26** Sibson, R. H. Rupture nucleation on unfavorably oriented faults. *Bull. Seism. Soc. Am.* **80**,  
268 1580–1604 (1990).
- 269 **27** Noda, H., Dunham, E. & Rice, J. R. Earthquake ruptures with thermal weakening and the  
270 operation of major faults at low overall stress levels. *J. Geophys. Res.* **114**, B07302 (2009).
- 271 **28** Toth, J. & Gurnis, M. Dynamics of subduction initiation at pre-existing fault zones. *J. Geophys.*  
272 *Res.* **103**, 18053–18067 (1998).
- 273 **29** Sobolev, S. V. & Babeyko, A. Y. What drives orogeny in the Andes? *Geology* **33**, 617–620  
274 (2005).
- 275 **30** Stern, R. J. & Gerya, T. Subduction initiation in nature and models: A review. *Tectonophysics*  
276 **746**, 173–198 (2018).
- 277 **31** Gephart, J. W. & Forsyth, D. W. An improved method for determining the regional stress  
278 tensor using earthquake focal mechanism data: Application to the San Fernando earthquake  
279 sequence. *J. Geophys. Res.* **89**, 9305–9320 (1984).
- 280 **32** Michael, A. J. Use of focal mechanisms to determine stress: a control study. *J. Geophys. Res.*  
281 **92**, 357–368 (1987).
- 282 **33** Rivera, L. & Kanamori, H. Spatial heterogeneity of tectonic stress and friction in the crust.  
283 *Geophys. Res. Lett.* **29**, 12–1 (2002).
- 284 **34** Ross, Z. E. *et al.* Hierarchical interlocked orthogonal faulting in the 2019 Ridgecrest earthquake  
285 sequence. *Science* **366**, 346–351 (2019).
- 286 **35** Hauksson, E. & Jones, L. Seismicity, stress state, and style of faulting of the Ridgecrest-Coso  
287 region from the 1930s through 2019: Seismotectonics of an evolving plate boundary segment.  
288 *Bull. Seism. Soc. Am.* **110**, 1457–1473 (2020).
- 289 **36** Jin, Z. & Fialko, Y. Finite slip models of the 2019 Ridgecrest earthquake sequence constrained  
290 by space geodetic data and aftershock locations. *Bull. Seism. Soc. Am.* **110**, 1660–1679 (2020).
- 291 **37** Dokka, R. K. & Travis, C. J. Role of the Eastern California shear zone in accommodating  
292 Pacific-North American plate motion. *Geophys. Res. Lett.* **17**, 1323–1327 (1990).

- 293 **38** Nur, A., Ron, H. & Beroza, G. The nature of the Landers-Mojave earthquake line. *Science*  
294 **261**, 201–203 (1993).
- 295 **39** McClusky, S. *et al.* Present day kinematics of the Eastern California Shear Zone from a geode-  
296 tically constrained block model. *Geophys. Res. Lett.* **28**, 3369–3372 (2001).
- 297 **40** Tymofyeyeva, E. & Fialko, Y. Mitigation of atmospheric phase delays in InSAR data, with  
298 application to the Eastern California Shear Zone. *J. Geophys. Res.* **120**, 5952–5963 (2015).
- 299 **41** Fialko, Y. & Jin, Z. On the origin of cross-faults responsible for the 2019 Ridgecrest, California,  
300 earthquake sequence. *Nature Geoscience* submitted (2020).
- 301 **42** Yang, W., Hauksson, E. & Shearer, P. M. Computing a large refined catalog of focal mechanisms  
302 for southern California (1981–2010): Temporal stability of the style of faulting. *Bull. Seism.*  
303 *Soc. Am.* **102**, 1179–1194 (2012).
- 304 **43** DuRoss, C. B. *et al.* Surface displacement distributions for the July 2019 Ridgecrest, California,  
305 earthquake ruptures. *Bull. Seism. Soc. Am.* **110**, 1400–1418 (2020).
- 306 **44** Yang, W. & Hauksson, E. The tectonic crustal stress field and style of faulting along the Pacific  
307 North America Plate boundary in Southern California. *Geophys. J. Int.* **194**, 100–117 (2013).
- 308 **45** Fialko, Y. & Simons, M. Deformation and seismicity in the Coso geothermal area, Inyo County,  
309 California: Observations and modeling using satellite radar interferometry. *J. Geophys. Res.*  
310 **105**, 21781–21793 (2000).
- 311 **46** Sykes, L. R. Intraplate seismicity, reactivation of preexisting zones of weakness, alkaline mag-  
312 matism, and other tectonism postdating continental fragmentation. *Reviews of Geophysics* **16**,  
313 621–688 (1978).
- 314 **47** Mitchell, E., Fialko, Y. & Brown, K. M. Velocity-weakening behavior of Westerly granite at  
315 temperature up to 600° C. *J. Geophys. Res.* **121**, 6932–6946 (2016).
- 316 **48** Fialko, Y., Rivera, L. & Kanamori, H. Estimate of differential stress in the upper crust from  
317 variations in topography and strike along the San Andreas fault. *Geophys. J. Int.* **160**, 527–532  
318 (2005).
- 319 **49** Wessel, P., Smith, W. H. F., Scharroo, R., Luis, J. & Wobbe, F. Generic Map-  
320 ping Tools: Improved Version Released. *Eos, Trans. AGU* **94**, 409–410 (2013). URL  
321 <http://onlinelibrary.wiley.com/doi/10.1002/2013E0450001/abstract>.

## Figures

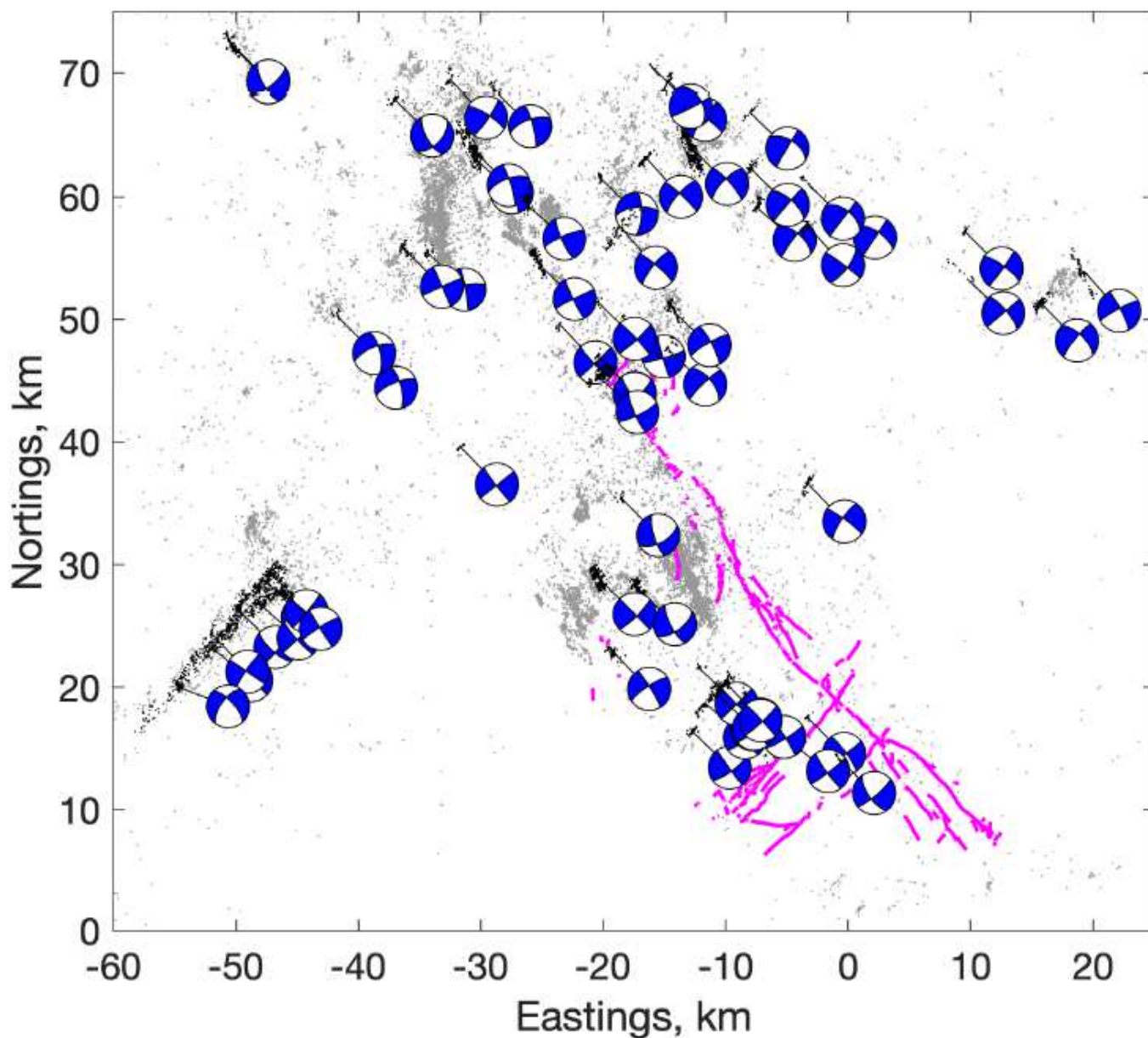
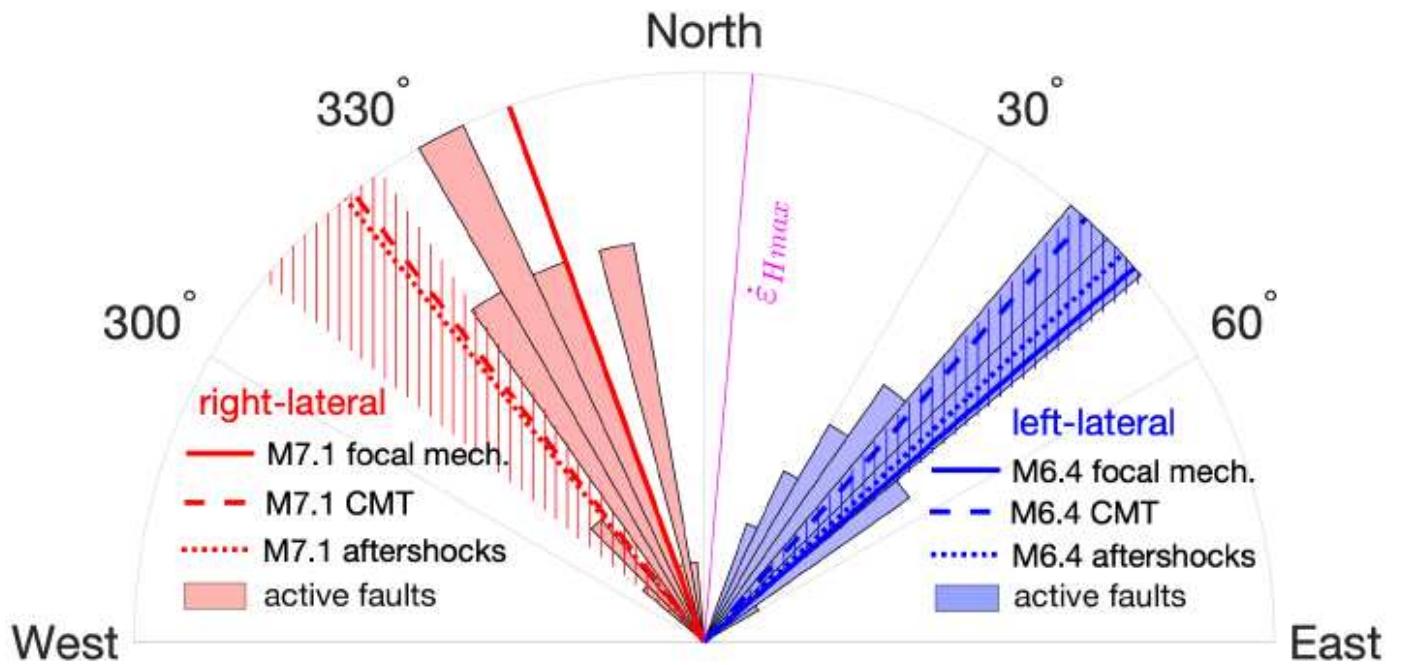


Figure 1

Map of the Ridgecrest-Coso area. Magenta wavy lines denote surface traces of the 2019 ruptures mapped by field surveys<sup>43</sup>. Grey dots denote pre-earthquake (1981-2019) seismicity from the focal mechanism catalog<sup>42</sup>. Black dots denote seismicity lineations selected by the clustering algorithm (see Supplementary Materials and Figures S2-S4 for details). White and blue “beach balls” denote the best-fitting double-couple composite focal mechanism for the respective linear clusters of earthquakes. Local origin is at 117.5°W, 35.5°N.



**Figure 2**

A distribution of strikes of 65 active fault segments shown in Figure 1. Red his-togram corresponds to right-lateral faults (total of 28 samples, maximum number of samples per bin: 7), and blue histogram corresponds to left-lateral faults (total of 37 samples, max-imum number of samples per bin: 9). Hatched areas denote orientation of faults ruptured by the M6.4 foreshock and M7.1 mainshock of the 2019 sequence<sup>36,41</sup>. Thin magenta line denotes the principal shortening rate axis derived from secular GPS velocities<sup>41</sup>.

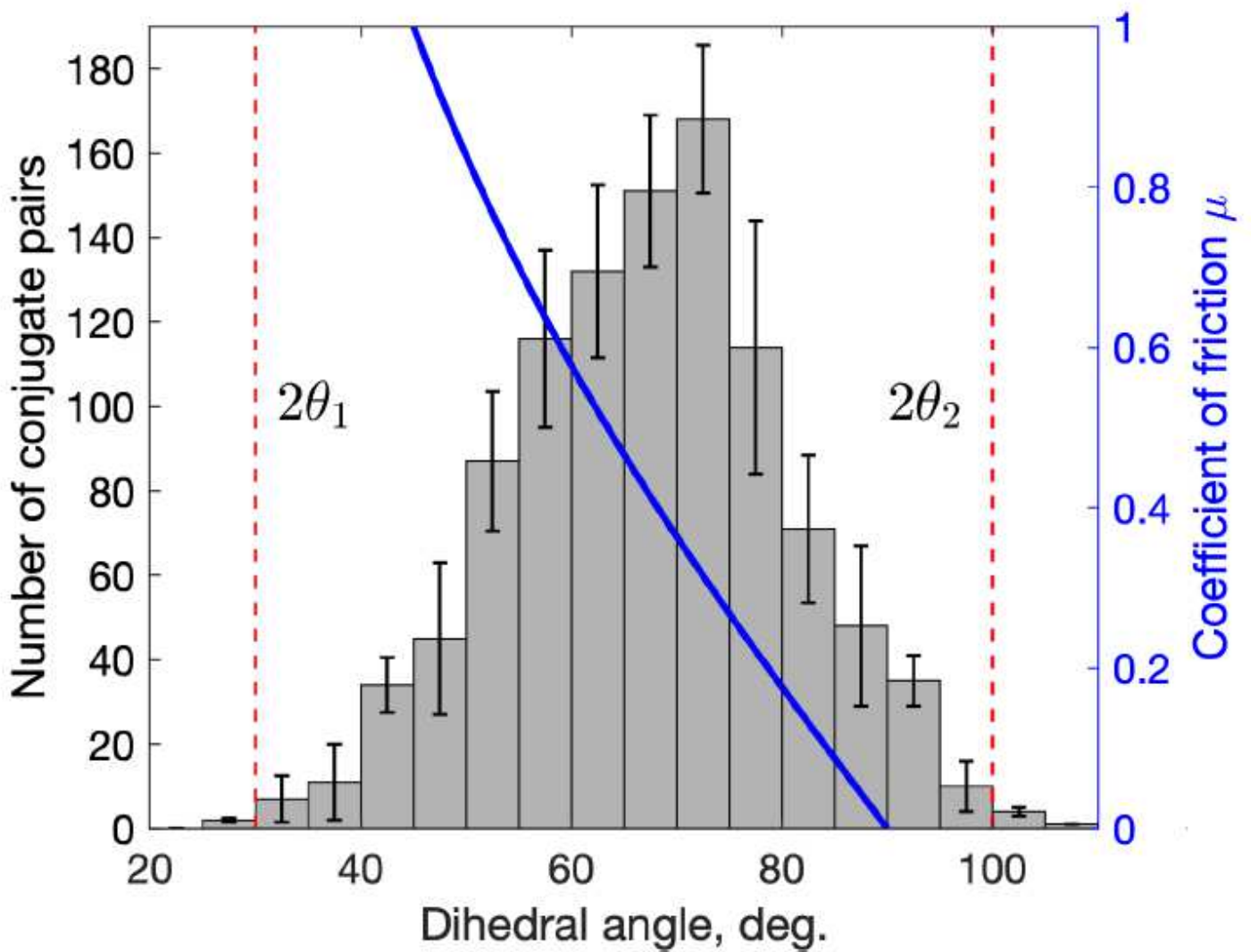
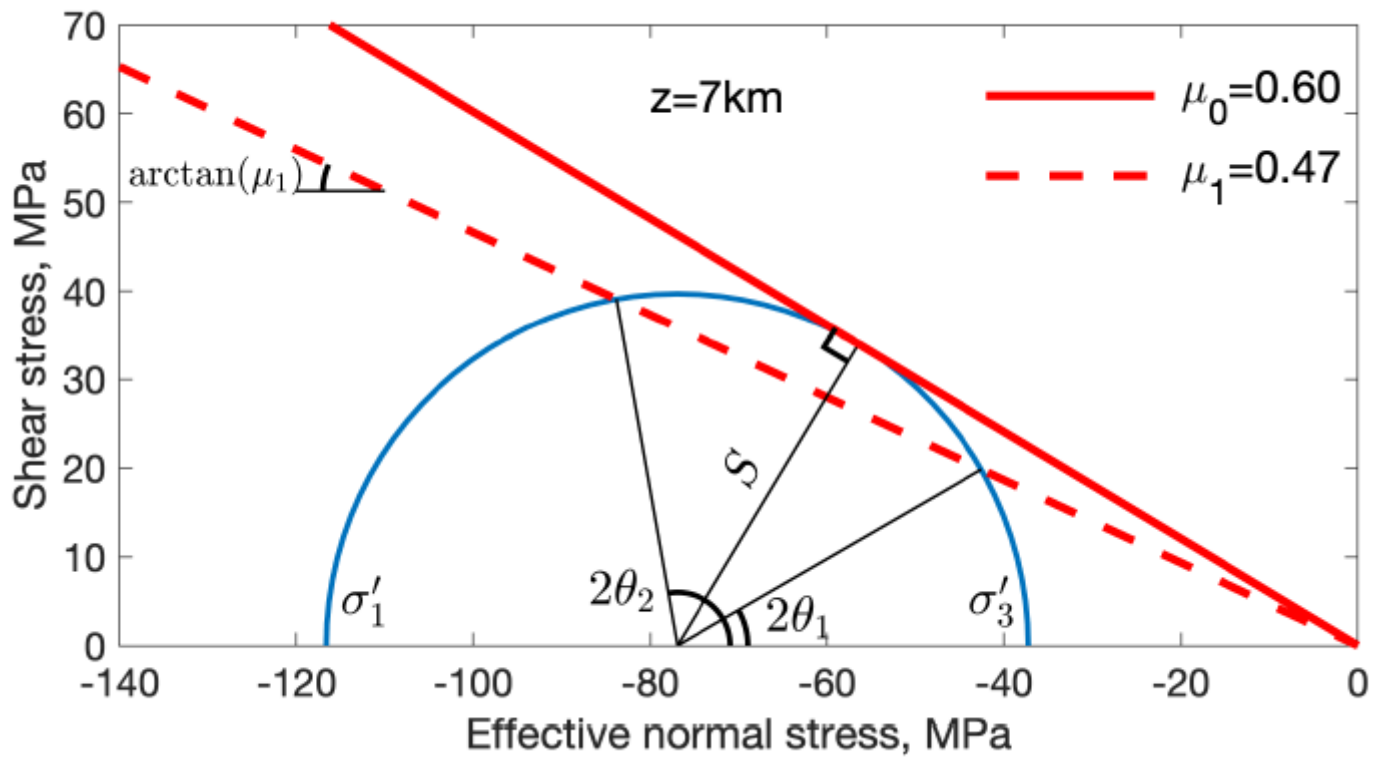


Figure 3

A histogram of dihedral angles between the conjugate strike-slip faults identified in Figure 1. Red vertical lines denote the lower ( $2\theta_1$ ) and upper ( $2\theta_2$ ) bounds on the observed distribution. Blue line (right axis) denotes the coefficient of friction corresponding to conjugate faults that are optimally oriented for failure according to the Mohr-Coulomb criterion,  $\mu = 1/\tan(2\theta)$ .



**Figure 4**

The estimated state of stress in the hypocentral region of the 2019 Ridgecrest earthquakes. Blue curve (the Mohr circle) denotes variations in shear stress on potential slip planes as a function of a dihedral angle  $2\theta$  between conjugate slip planes (or angle  $\theta$  between a slip plane and the maximum compression axis). Radius of the Mohr circle represents the maximum shear stress,  $S = |\sigma_1 - \sigma_3|/2$ . Red lines are the Mohr-Coulomb failure envelopes corresponding to activation of pre-existing faults ( $\mu_1$ , dashed line), and generation of new faults ( $\mu_0$ , solid line). Calculations assume  $\rho_c = 2.7 \times 10^3 \text{ kg/m}^3$ ,  $\rho_w = 103 \text{ kg/m}^3$ , and  $g = 9.8 \text{ m/s}^2$ .

## Supplementary Files

This is a list of supplementary files associated with this preprint. Click to download.

- [SMN.pdf](#)